Self-Aligned Focusing Schlieren and OH Planar Laser-Induced Fluorescence Flow Visualization in a Dual-Mode Scramjet

Brett F. Bathel*, Joshua M. Weisberger†, and Wayne E. Page Jr.‡
NASA Langley Research Center, Hampton, Virginia, 23681

Andrew J. Metro§, Robert D. Rockwell¶, and Chloe E. Dedic‖
University of Virginia, Charlottesville, Virginia, 22904

Nicholas A. Mejia** and Bryan E. Schmidt††
Case Western Reserve University, Cleveland, Ohio, 44106

A high-speed self-aligned focusing schlieren (SAFS) system was used to visualize density gradients in and around the cavity flameholder of the combustor section of the University of Virginia Supersonic Combustion Facility (UVASCF). Images with this system were acquired at a framing rate of 110 kHz with no fuel injection, with fuel injection but no flame, and for fuel injection with combustion corresponding to a global equivalence ratio of $\phi = 0.18$. Images with an air throttle in operation to modify the shock train location with fuel injection and with flame were also acquired. Simultaneous OH planar laser-induced fluorescence (PLIF) images were also acquired at a framing rate of 20 Hz. Results obtained with both visualization techniques are compared to one another to highlight how SAFS can complement more advanced flow visualization techniques and resolve dynamic behavior that may not otherwise be captured. Both proper orthogonal decomposition (POD) and dynamic mode decomposition (DMD) analysis techniques are applied to the SAFS image sequences to identify coherent periodic structures for the runs with fuel injection and combustion.

I. Introduction

Non-intrusive optical diagnostics can provide critical information about in-flow behavior in the harsh environment of a scramjet combustor where physical probes may not survive and affect the very properties they are trying to measure. At the University of Virginia Supersonic Combustion Facility (UVASCF), numerous non-intrusive flow visualization diagnostics have been implemented to study the flow characteristics in the cavity flameholder of the combustor section. Hydroxyl (OH) [1–8] and formaldehyde (CH_2O) [5, 9, 10] planar laser-induced fluorescence (PLIF) measurements have been made to visualize combustion intermediates and products with relatively high-spatial resolution. Broadband [11], CH* [9], and OH* [8] chemiluminescence has also been previously performed for this purpose, although these measurements represent an integrated view of the emitting species along the camera's line-of-sight.

Conventional focusing schlieren measurements were performed in the UVASCF by Kouchi et *al*. [12, 13]. Unlike conventional schlieren, which provides a path-integrated view of the density gradient field, conventional focusing schlieren (like that developed by Hartmann [14], Schardin [15], and Burton [16] and later modernized by Weinstein [17]) can filter out non-pertinent artifacts and flow features away from the plane of focus. Ideally, this includes filtering out the effects of the spatially-varying refractive index of windows, usually caused by the thermal and mechanical stress imparted to the windows while the tunnel is in operation. These appear as non-uniform bright and dark regions in a conventional schlieren image, potentially obscuring relevant flow information. Depending upon the optical configuration, focusing schlieren can provide images of density gradients over a plane with small depth-of-focus, approaching the

*Research Engineer, Advanced Measurements and Data Systems Branch, MS 63, AIAA Senior Member.
†Research Engineer, Advanced Measurements and Data Systems Branch, MS 63, AIAA Senior Member.
‡Pathways Graduate Student, Advanced Measurements and Data Systems Branch, MS 63, AIAA Student Member.
§Graduate Research Assistant, Department of Mechanical and Aerospace Engineering, AIAA Student Member.
¶Senior Scientist, Department of Mechanical and Aerospace Engineering, AIAA Member.
‖Assistant Professor, Department of Mechanical and Aerospace Engineering, AIAA Senior Member.
**Graduate Research Assistant, Mechanical and Aerospace Engineering, 2123 Martin Luther King Jr. Drive, AIAA Student Member.
††Assistant Professor, Mechanical and Aerospace Engineering, 2123 Martin Luther King Jr. Drive, AIAA Senior Member.

spatial resolution of PLIF methods (i.e., laser sheet thickness). However, conventional focusing schlieren requires a precise and time-consuming alignment procedure to be performed, and does not allow for quick adjustments to be made to the system once alignment is complete. The system is also sensitive to vibrations, which result in misalignment of the system and, subsequently, loss of signal. General details on conventional focusing schlieren can be found in the book by Settles [18].

In this work, a novel self-aligned focusing schlieren (SAFS) system [19, 20] is used to visualize the density gradients resulting from fuel injection and across the cavity-induced shear layer in the UVASCF combustor. Since the instrument is inherently self-aligned, the setup time is significantly reduced relative to that of conventional focusing schlieren systems and its signal is insensitive to vibrations. The footprint of the instrument is also much more compact than that of a conventional focusing schlieren system, allowing for greater flexibility when testing in space-constrained environments. The current work presents focused schlieren images obtained at a framing rate of 110 kHz that are compared to images obtained alongside OH PLIF system operating at 20 Hz. The acquisition of both image types demonstrates how SAFS can complement other advanced optical diagnostics and provide unique insight into flow phenomena that may not be captured using other techniques.

II. Experimental Setup

A. Self-Aligned Focusing Schlieren

Figure 1a shows a schematic of the SAFS system as implemented at the UVASCF. Here, incoherent 40 ns laser pulses from a Cavitar Cavilux HF light source operating at 640 nm were loosely collimated and diffused by a condensing/diffusing lens, CD. The light was then passed through a linear polarizer, LP^1, that only transmitted linear vertically polarized, LVP, light. This light was then reflected onto the instrument's optical axis by a polarizing beamsplitter, PBS, and subsequently passed through a Ronchi Ruling, RR, with a frequency of 2 line pairs per mm (lp/mm). The light then passed without refraction through a polarizing Rochon prism, RP, and an $f = 80 - 200$ mm zoom field lens, FL, was used to form an image of the RR onto a retroreflective background, RBG, on the opposing side of the combustor test section. Prior to the light being incident on the RBG, it passed through a thin sheet of quarter-wave film, QWF, that modified the incident light from LVP to right-circularly polarized, or RCP, light. Upon retroreflection from the RBG, the orientation of the RCP light changed to left-circularly polarized, or LCP, light. Now, when passing back through the QWF, it was modified to linear horizontally polarized, LHP, light.

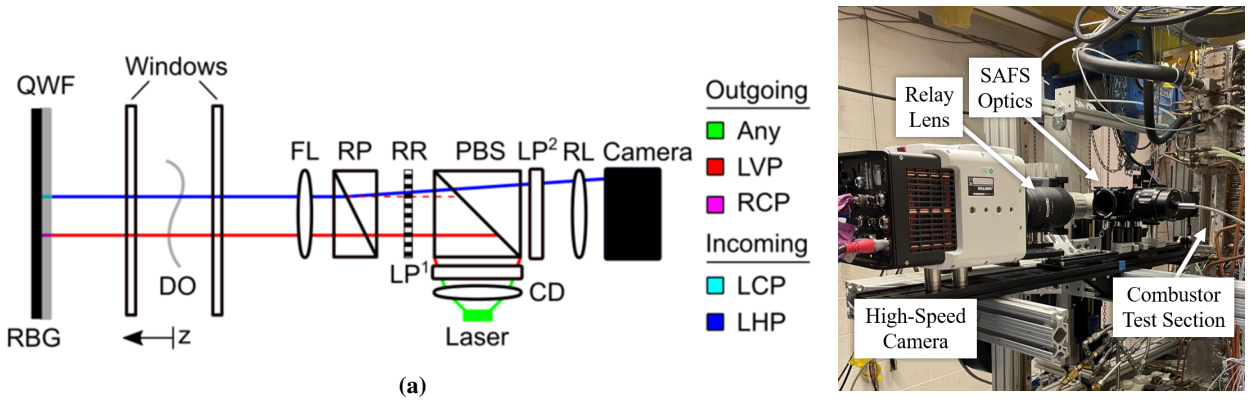
After a return pass through the test section, the FL formed an image of the RR projection back onto the RR. However, since the returning light was LHP, the RP refracted the light 0.125°. This resulted in a small offset between the RR and the reimaged projection of the RR, resulting in the schlieren cutoff effect. Since the light was LHP, it was allowed to pass through the PBS and a second linear polarizer, LP^2, with its transmission axis aligned in the horizontal direction to improve contrast when imaged by the camera with attached relay lens, RL.

A high-speed Phantom TMX 7510 camera with a 105 mm RL was used to image the resulting focused schlieren images. The camera was operated at a framing rate of 110 kHz with a 4 μs exposure and a 1024×512 pixel resolution (less than the full 1280×800 pixel resolution to enable the higher framing rate) with a magnification of 26.05 pixels/mm with a pixel size of 18.5 μm. The entire SAFS system was mounted on a rail structure that could be translated in three orthogonal directions to provide adjustment in the position of the instrument, and thus the field-of-view. Figure 1b shows the system mounted to this structure.

B. OH Planar Laser-Induced Fluorescence

For the OH PLIF measurements, 8 ns laser pulses from a Spectra Physics Nd:YAG laser operating at 20 Hz and a wavelength of 1064 nm were frequency doubled to 532 nm with a second harmonic generator. A Sirah Cobra Stretch dye laser was then pumped with this light resulting in an output wavelength of 566 nm. This 566 nm beam from the dye laser was then frequency doubled to achieve an output of 283 nm pulsed laser light used to excite the $Q_1(8)$ transition of the $A^2\Sigma^+ \rightarrow X^2\Pi(1,0)$ band of OH. A periscope was used to direct the beam to a set of sheet-forming optics and subsequently into the combustor test section, as shown in Fig. 2.

Images of the resulting OH fluorescence were captured by an intensified PI-MAX4 1024i camera. A Cerco UV-transmitting lens with a focal length of f =100 mm and f/number setting of 5.6 was attached to the camera via a LaVision Scheimpflug mount. A bandpass filter (Semrock, FF02-320/40-30-D) was placed in front of the camera lens to reject laser scatter from the laser sheet inside the test section. A total of 198 OH PLIF images were acquired per



(a) (b)

Fig. 1 (a) Schematic of the self-aligned focusing schlieren system and (b) an image of the system mounted in the UVASCF. Components include a condenser-diffuser lens, CD; linear polarizer, LP; polarizing beamsplitter, PBS; Ronchi ruling, RR; Rochon prism, RP; field lens, FL; density object, DO; quarter-wave plate, QWP; retroreflective background, RBG; and relay lens, RL.

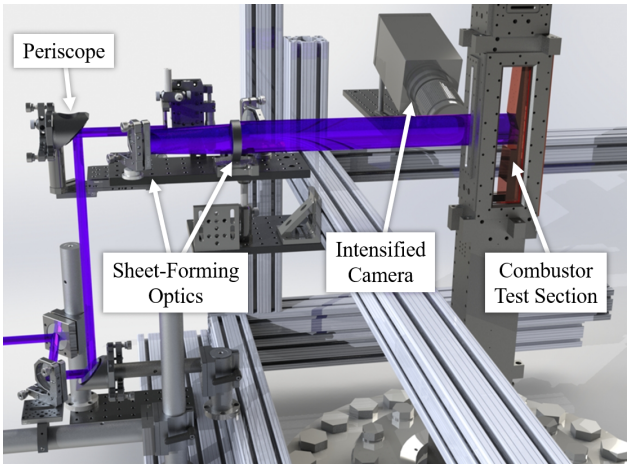


Fig. 2 Rendering of the OH PLIF setup about the combustor test section.

condition, with background subtraction from an average of 100 PLIF images with the laser sheet blocked.

C. UVASCF Combustor Test Section

Figure 3a includes a schematic of the UVASCF tunnel flow path. The top portion of this schematic shows a side view of the tunnel flow path, while the bottom portion shows a top view. The tunnel is electrically heated to 1200 K. Conditions in the tunnel were set to approximate an M = 5 flight enthalpy condition. The facility provides a continuous M = 2 flow that exits the nozzle. For this test, ethylene (C_2H_4) fuel was injected through the middle row of injectors shown in Fig. 3b, with each row having five individual injectors each with a diameter of 0.53 mm. This geometry is similar to Modified Configuration E of the UVASCF; further information can be found in Ref. [21]. Figure 3a (Side View) shows the location of the air throttle, which consists of two high-pressure air injectors which allow for back-pressurization to alter the pre-combustor shock train's position.

The SAFS camera field-of-view required to resolve turbulent flow structures with sufficient spatial and temporal resolution was limited to a rectangular plane spanning W = 39.3 mm in the streamwise direction and H = 19.7 mm in the cavity floor-normal direction. To capture images of fuel injection, cavity flow, and ramp flow, the rail hardware upon which the SAFS system (and PLIF system) was mounted was translated to three points in the streamwise and floor-normal directions. The upstream-most field-of-view, denoted as position 1a, provided a view of the flow structures

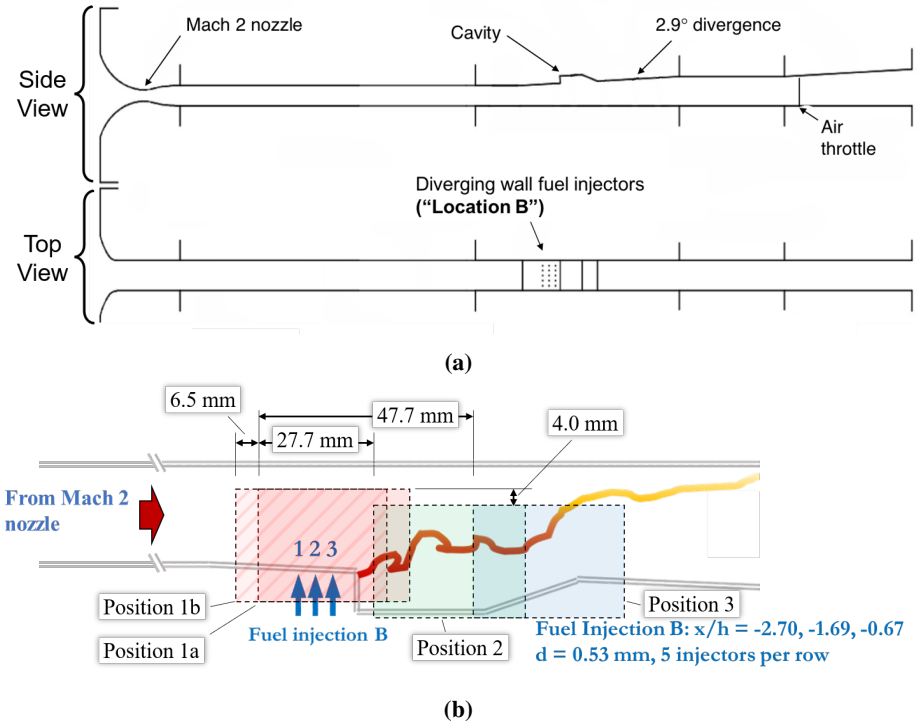


Fig. 3 (a) Schematic of tunnel flow path indicating relative location of combustor cavity and fuel injectors used in this test. The top portion of this image shows a side view of the flow path, while the bottom portion shows a top view of the flow path. (b) Zoomed in view of combustor cavity showing relative fuel injector locations and the approximate location of the overlapping SAFS fields-of-view: position 1a (red), position 1b (striped red), position 2 (green), and position 3 (blue).

from the B2 fuel injectors, which were imaged near the left-hand side of the field-of-view. This field-of-view is denoted by the red region in Fig. 3b. For one of the runs presented in this work, a second field-of-view, denoted as position 1b, was obtained by translating the hardware 6.5 mm upstream of position 1a so that the B2 row of fuel injectors were centered in the images. This field-of-view is denoted by the red striped region in Fig. 3b. The hardware was then translated 24.1 mm downstream and 4.0 mm down (with respect to the cavity floor-normal direction) relative to position 1a, denoted as position 2. Position 2 was used to capture images of flow structures within the combustor cavity and is represented by the green region shown in Fig. 3b. Finally, the hardware was translated 47.7 mm downstream and 4.0 mm down relative to position 1a, denoted as position 3, to capture flow structures above the ramp at the aft portion of the combustor cavity. Position 3 is represented by the blue region in Fig. 3b. Note that for all runs, the focal plane of the SAFS instrument was fixed at the combustor's spanwise axis of symmetry. The OH PLIF camera hardware was also mounted to the same hardware to capture similar fields-of-view to that obtained with the SAFS system.

III. Image Processing

A. Self-Aligned Focusing Schlieren Images

After testing was completed, images of a calibration target consisting of a regular 2D pattern of white dots on a black background were acquired in the SAFS focal plane. These images were loaded into LaVision's DaVis 10 software package and a spatial scale of 26.05 pixels/mm obtained. While the SAFS camera field-of-view spanned W×H = 39.3-mm×19.7-mm, the intensity pattern provided by the pulsed light source was not uniform over this region. Figure 4a shows raw single-shot images captured during a fuel-on, flame-on run condition with an equivalence ratio of $\phi = 0.18$ at positions 1a, 2, and 3 (proceeding from left to right). To improve schlieren contrast, a time-average image from each position was computed from a sequence of 4096 sequential single-shot images in MATLAB. This

time-average image was then subtracted from each single-shot image and the *wiener2* adaptive low-pass filter function with a 5×5-pixel window used to estimate the local image mean and standard deviation. A mask was then applied to remove regions of the image obscured by the test section as well as regions with low signal-to-noise. Note that near the B2 row of injectors, the mask appears uneven, but the floor of the test section at this point was continuous. The images from each camera position were then cropped to encompass the unmasked regions. Finally, the maximum and minimum pixel intensity from image sequences were obtained and the intensity scaled by the subtracting the global minimum intensity value from all single-shot images and then normalizing the images by the difference between the global maximum and minimum values. The resulting processed images are shown in Fig. 4b, with positions 1a, 2, and 3 arranged from left to right.

Once the single-shot images were processed, they were stitched together using the MATLAB 2D linear interpolation function *interp2*. This created a single image with an interpolated resolution approximately a factor of 2 higher than that of the original images as shown in Fig. 4c. Here the red, green, and blue regions correspond to camera positions 1a, 2, and 3, respectively. To create a smooth transition between overlapping field-of-view regions (such as the yellow region between positions 1a and 2 and the cyan region between position 2 and 3 in Fig. 4c), weighting functions were applied to the overlapping regions of the single-shot images. In these weighting functions, the pixel intensity values from the upstream camera position from each single-shot image were varied linearly from 1 to 0 proceeding in the downstream direction. Conversely, pixel intensity values from the downstream camera position from each single-shot image varied linearly from 0 to 1 proceeding in the downstream direction. The weighted intensities from each camera position were then summed together in these regions. Figure 4d shows an image obtained using this stitching method from the fuel-on, flame-on run, composed of the single-shot images of Fig. 4b.

B. Modal Analysis Techniques

1. Proper Orthogonal Decomposition

The proper orthogonal decomposition (POD) is a data-driven algorithm capable of extracting spatially orthogonal modes ranked by their contribution to the variance in the data and has long been used within the fluid mechanics community [22]. One of the earliest applications in this field came from Bakewell and Lumley in the field of turbulence and originated with an attempt to find a set of deterministic functions that captured the total kinetic energy of the flow [23]. These functions, or modes, can provide insight into how the most important flow features evolve as test conditions vary and ideally are direct spatial representations of coherent structures in the flow. The robustness of the POD comes from its procedural linearity while making no assumptions on the linearity of the problem, and has been used to analyze turbulent flows, wall bounded flows, convection, supersonic retropropulsion, and stagnation-point injection, among others [24–28].

2. Dynamic Mode Decomposition

A powerful tool for representing dynamical systems is the dynamic mode decomposition (DMD) [29]. The DMD is an eigendecomposition of an approximation to the Koopman operator, a linear, infinite dimensional operator that represents nonlinear, finite-dimensional dynamics. The resulting eigenvectors are spatiotemporal modes that represent spatially correlated structures that oscillate at a fixed frequency [30]. Unlike the POD, the original DMD algorithm does not give an optimal ranking of modes as it pertains to flow reconstruction and choosing the optimal modes is often nontrivial [22, 31, 32]. In order to address this shortfall, many variants of DMD have been introduced in order to both optimize and rank the DMD modes by various preprocessing, post-processing, and algorithmic adjustments [33–38]. A thorough review of DMD, its relation to the Koopman operator, and many variants of the algorithm that have been developed can be found in Ref. [39] and a general review of modal analysis for fluid flows can be found in Ref. [22].

In this study, the POD and DMD were performed on the SAFS data in order to identify dominant structures in the flow field and their associated temporal dynamics. Each image sequence contains 4096 SAFS snapshots in time with the length scale of 38.38 μm/pixel, sampled at 110 kHz. A randomized linear algebra method described by Erichson *et al.* was used to reduce the rank of the data matrix to 50 modes [40] in order to increase computation speed and reduce the memory requirement. The POD was first used to find the variance-ranked spatially orthogonal modes and their associated frequency content, after which the DMD modes were analyzed with a combination of the sparsity-promoting algorithm by Jovanic *et al.* and the DMD ranking criterion of Kou and Zhang [31, 32]. Additionally, some DMD modes that occurred at frequencies matching those of the POD spectra were analyzed.

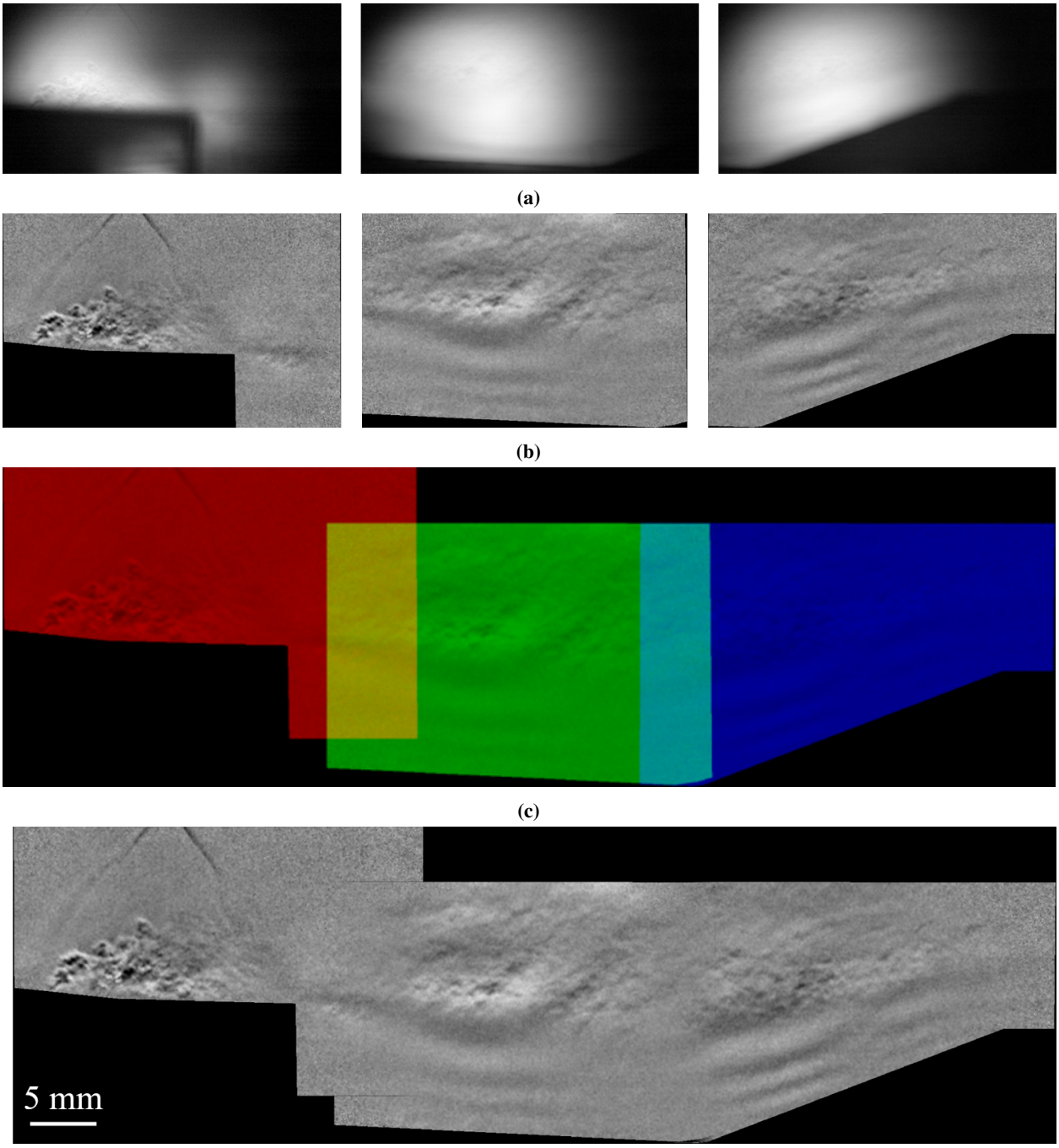


Fig. 4 (a) Single-shot raw images at camera positions 1a, 2, and 3 (left to right), (b) processed single-shot images showing masked regions in black, (c) overlapping camera positions from positions 1a (red), 2 (green), and 3 (blue), and (d) final stitched image for fuel-on, flame-on condition with $\phi = 0.18$.

In the POD or DMD results from schlieren image sequence data, the color mapping is representative of the correlation between changing intensities in the image. The color map used in this work ranges from dark blue, to white, to dark red, with white indicating regions that are uncorrelated with any other region in the image. Blue and red regions are then correlated with other blue and red regions, respectively, and anti-correlated with other red and blue regions, respectively. In general, this is used to interpret the intensity variations, and therefore in many instances, motion, corresponding to

density gradient structures in the images.

IV. Results

SAFS image sequences were acquired for four different run conditions: flow with no fuel injection or flame (Fuel-Off, Flame-Off), flow with fuel and no flame (Fuel-On, Flame-Off), flow with both fuel injection and flame (Fuel-On, Flame-On), and with both fuel injection and flame with an air throttle (Air Throttle). The air throttle in this work consisted of room-temperature air injection downstream of the combustor cavity that was used to control back pressure in the test section and shock train position upstream of the cavity. OH PLIF image sequences were acquired for the Fuel On, Flame On and Air Throttle cases.

A. Fuel-Off, Flame-Off

Figure 5 shows a stitched SAFS single-shot image taken from a sequence of 4096 images with no fuel injection and no combustion. The position 1b, 2, and 3 fields-of-view were used to generate this image. The purpose of capturing this sequence was to observe the baseline flow in the combustor. In these images, a shear layer that initiates above the cavity downstream of the injectors is observed, as is a region of recirculating flow above the floor of the cavity. While not apparent in this single-shot image, the full sequence of images show intermittent oblique shock structures that appear to reflect from the ceiling of the combustor near the center of the image (within the position 2 field-of-view). Additional intermittent oblique shock structures emanating above the cavity ramp from the shear layer are also observed.

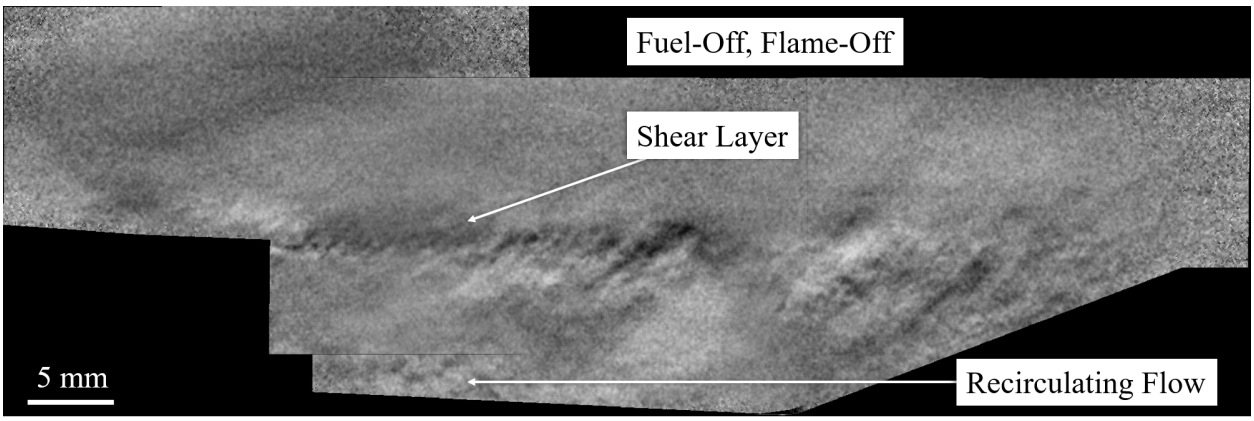


Fig. 5 Stitched single-shot image from a sequence of 4096 single-shot images acquired with no fuel injection and no flame.

B. Fuel-On, Flame-Off

Figure 6 shows a stitched SAFS single-shot image taken from a sequence of 4096 images with fuel-on, flame-off. The fuel injection rate for this run condition corresponded to a global equivalence ratio of $\phi = 0.18$ when running flame-on. The positions 1a, 2, and 3 fields-of-view were used to create the stitched image. In the full sequence of images, the injection of fuel results in the formation of a primary shock wave ahead of the point of injection as well as a secondary shock wave downstream of the point of injection, but upstream of the cavity location. Additional intermittent shocks are also observed above the injection fuel plume when viewing this full sequence. Further downstream, an unsteady reflected shock from the combustor ceiling is observed. Note that the black masked region where this reflected shock originates from is not the ceiling of the combustor, but represents the top extent of the fields-of-view for positions 2 and 3. Additional intermittent shocks emanating from the fuel plume above the cavity ramp are also observed in the full image sequence. As with the baseline fuel-off, flame-off condition, a region of recirculating flow above the cavity floor is observed.

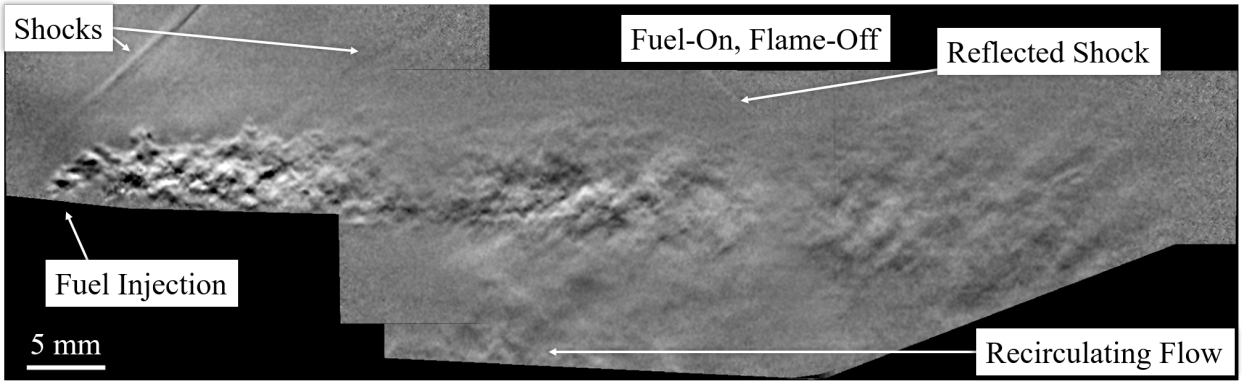


Fig. 6 Stitched single-shot image from a sequence of 4096 single-shot images acquired with fuel injection and no flame.

C. Fuel-On, Flame-On

1. Comparison of SAFS and OH PLIF Data

Figure 7 shows a stitched single-shot SAFS image of the fuel-on, flame-on run condition with a global equivalence ratio of $\phi = 0.18$. Here, the stitched image is composed of images captured from positions 1a, 2, and 3 fields-of-view. Compared to the fuel-on, flame-off image shown in Fig. 6, there are several notable differences observed. First, the signature of a strong reflected shock from the combustor ceiling is observed near the point of fuel injection. The reflected shock observed in the fuel-on, flame-off image above the cavity in Fig. 6 is no longer observed. Most notably, wave-like structures are observed within the cavity. These wave-like structures also intermittently develop nodal regions where the signature of the wave is not observed. Next, the recirculation flow region along the floor of the cavity has decreased in size. Finally, the signal from the plume above the cavity is significantly lower than was observed in the fuel-on, flame-off case. Presumably, this is a result of the increase in temperature due to combustion and, therefore, a reduction in density. With combustion, hot product gases may mix in with the gas in the primary flow path, resulting in a mixture with smaller gradients in density.

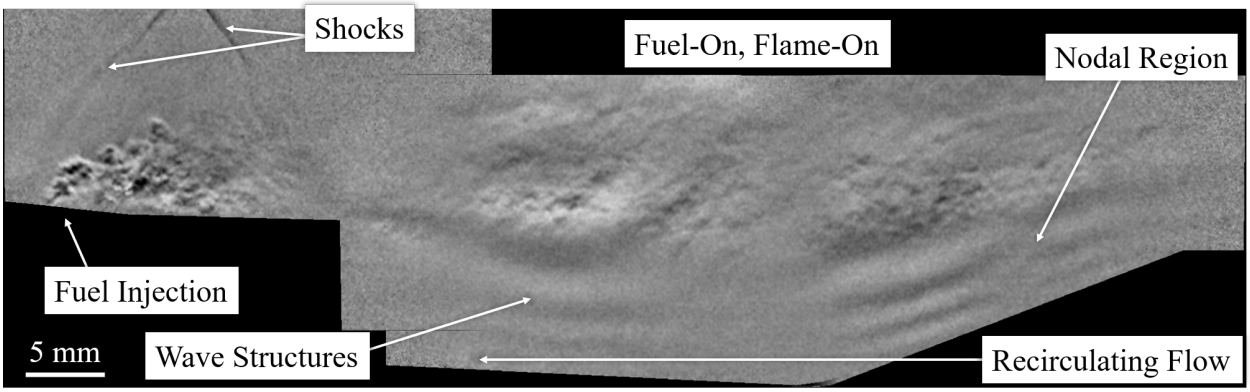
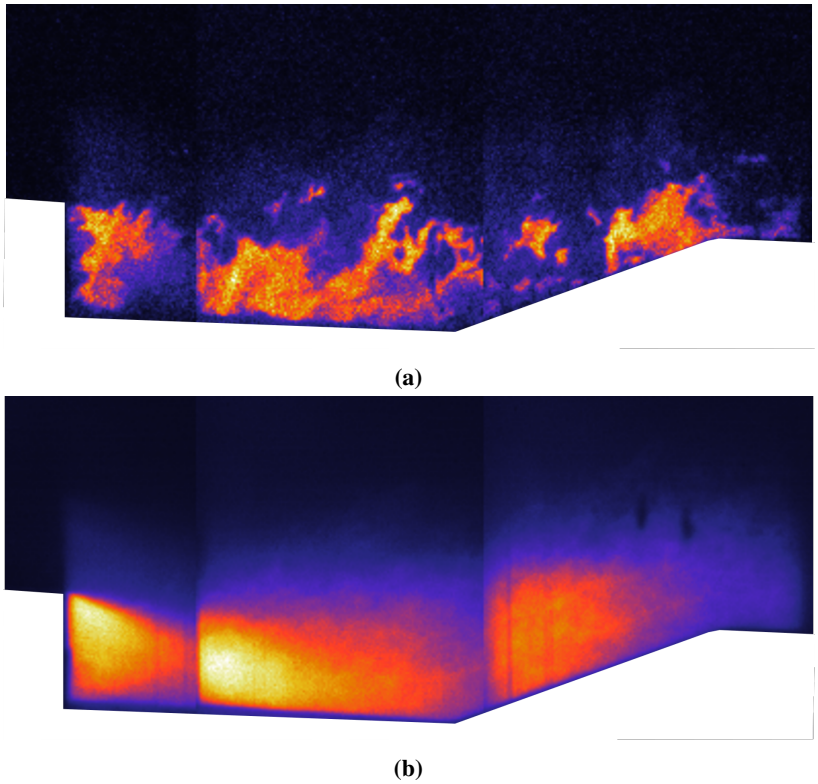


Fig. 7 Stitched single-shot image and from a sequence of 4096 single-shot images acquired with fuel injection and with flame.

Figure 8a shows an OH PLIF image stitched together from positions 1a, 2, and 3 fields-of-view. Notably, multiple flame edges are observed within the cavity itself, beneath the shear layer, suggesting multiple flame edges occurring in the cavity itself. In this single-shot image, a non-uniform distribution of OH is observed primarily within the cavity. This is in contrast to the SAFS image in Fig. 7, where smooth wave-like structures were observed over the same extent. Figure 8b shows a stitched time-average of the OH PLIF images that show the OH is primarily contained to the combustor cavity except for a small region above the ramp, where it extends into primary combustor flow path. In this

image, the discontinuity in the intensity pattern between adjacent fields-of-view is a result of the laser sheet decreasing in intensity in the downstream direction, away from its center, which was towards the upstream part of the camera's field-of-view.



(a)

(b)

Fig. 8 Stitched (a) single-shot image and (b) time-average image from a sequence single-shot OH PLIF images acquired with fuel injection and with flame.

2. POD Analysis of SAFS Data

The energy fractions of the top ten POD modes for each camera position of the fuel-on, flame-on run condition are shown in Fig. 9. Here, the dominant mode in the POD of each camera position contains roughly the same energy fraction. The flow captured at the positions 1a and 2 fields-of-view have a larger drop in energy from mode one to two than that of the flow at position 3. For each of the camera positions, the POD modes seem to start to level off after mode three or four, so the discussion is limited to the top three modes again for brevity.

The POD mode with the most energy at the fuel-on, flame-on run condition for camera positions 1a, 2, and 3 is shown in Figs. 10a, 10b, and 10c, respectively with the associated frequency spectra. In each of the POD images large out of phase structures are present. In Fig. 10a, an oscillation that seems to stem from fuel oscillation dominates and is observed to be coupled with an oscillation in the shock. The oscillation seems to have split into two packets and there seem to be weakly correlated disturbances propagating downward to the test section wall as shown in Figs. 10b and c. The downward propagating wave-like structures in Fig. 10b seem to roughly be in phase with themselves for the camera at position 2, but there are clear out of phase wave-like structures in Fig. 10c at position 3. The spectra contains notable peaks at 28.5 kHz, 44.4 kHz, 48.9 kHz, and 55 kHz for the camera 1a position (a), 16.2 kHz, 17.9 kHz, 49 kHz, and 53.5 kHz for the camera 2 position (b), and 22.7 kHz, 24.9 kHz, 30.8 kHz, 33.8 kHz, and 45.6 kHz for position 3 (c). The spectra includes large peaks at 55 kHz, the Nyquist cutoff frequency.

The second-highest-energy POD mode at the fuel-on, flame-on run condition for camera positions 1a, 2, and 3 is shown in Figs. 11a, 11b, and 11c, respectively with the associated frequency spectra. Here, in Fig. 11a, an oscillatory structure associated with the injection site is seen. The flow observed at position 2 11b and position 3 11c show large scale oscillations similar to those seen in Fig. 10b and Fig. 10c. In Fig. 11b, the downward wave-like structures now

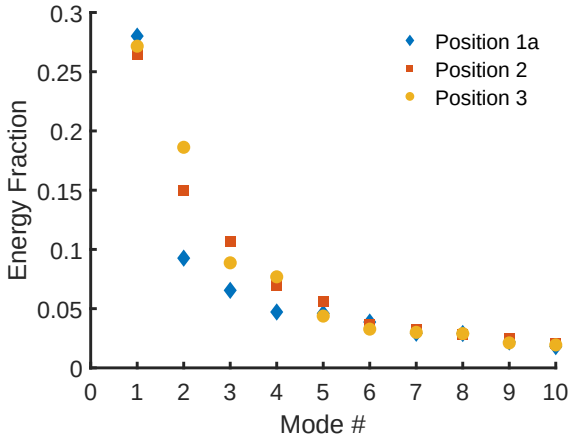


Fig. 9 Top ten POD mode energy fractions of each camera position of the throttle off tests.

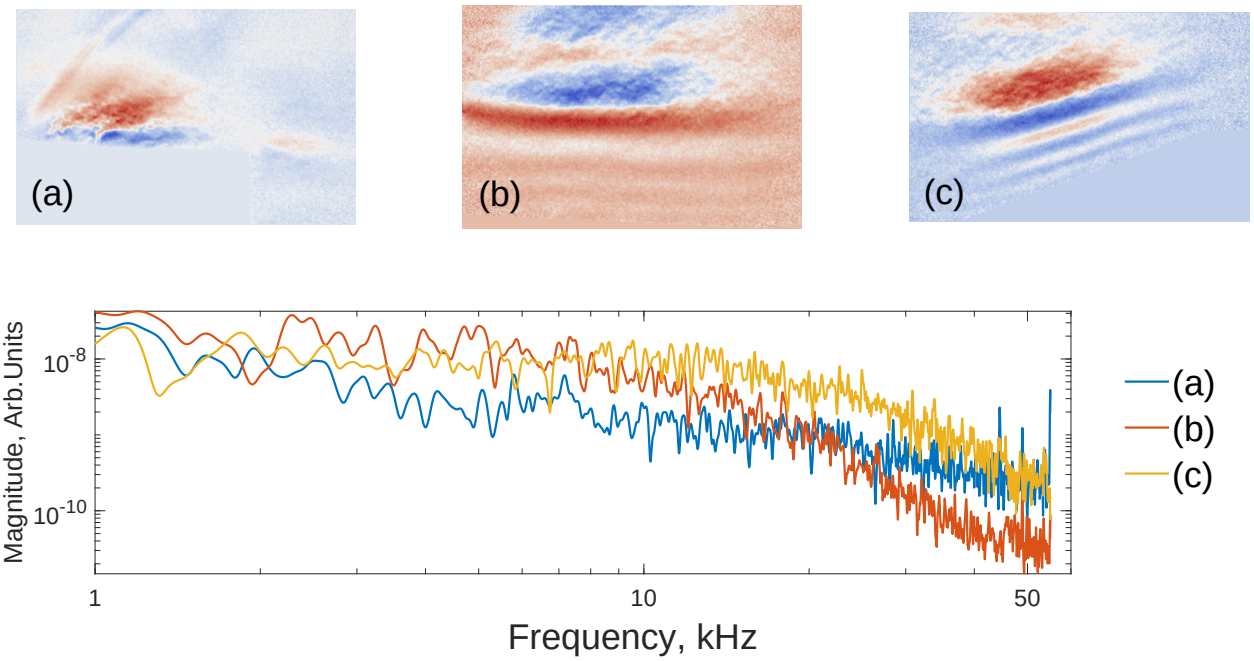


Fig. 10 Modes with highest energy in the fuel-on, flame-on run condition POD of the (a) camera 1a position, (b) camera 2 position, and (c) camera 3 position with the spectra given for each.

exhibit out of phase information while Fig. 11c is extremely similar to 10c in that there are out of phase wave-like structures propagating downward, but it notably is missing the phase information that is contained in the top of 10c. The spectra contains notable peaks at 2.5 kHz, 7 kHz, 21 kHz, 28.4 kHz, 44.5 kHz, 48.9 kHz, and 55 kHz for the camera 1a position (a), 13.3 kHz and 17.8 kHz for the camera at position 2 (b), and 18 kHz, 30.8 kHz, 33.8 kHz, and 45.6 kHz for the camera at position 3 (c).

The third-highest-energy POD mode at the fuel-on, flame-on run condition for camera positions 1a, 2, and 3 is shown in Figs. 12a, 12b, and 12c, respectively with the associated frequency spectra. Here, in Fig. 12a the mode shows a small disturbance near the injection site. Notably, the energy drop after this mode is relatively small so this mode could be mostly noise. In Fig. 12b there are again wave-like structures propagating downward. In Fig. 12c the oscillations in the flow are no longer large individual packets of similar phase information, but rather it seems there are two sets of waves split down the middle and translated half a wavelength vertically with respect to each other. The spectra contains notable peaks at 18.9 kHz, 50.6 kHz, and 55 kHz for the camera at position 1a (a), 18 kHz, 20.5 kHz, 48 kHz for the camera at position 2 (b), and 30.8 kHz and 33.8 kHz for the camera at position 3 (c).

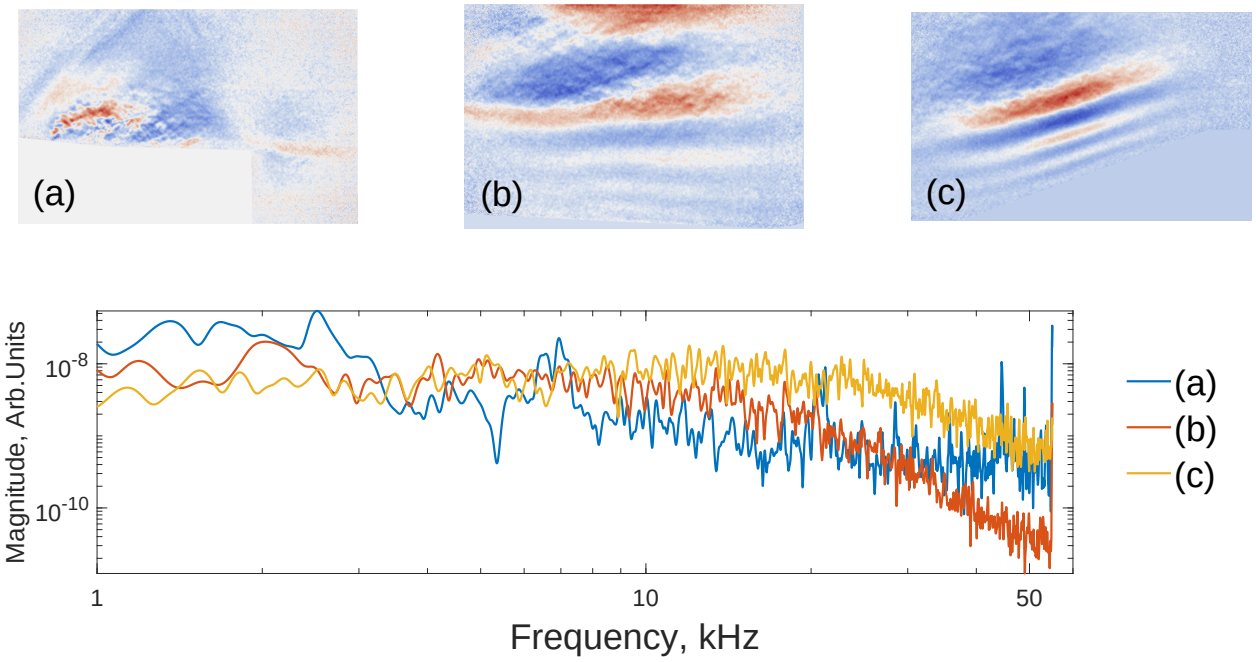


Fig. 11 Second-highest-energy mode in the POD of the (a) camera 1a position, (b) camera 2 position, and (c) camera 3 position with the spectra given for each.

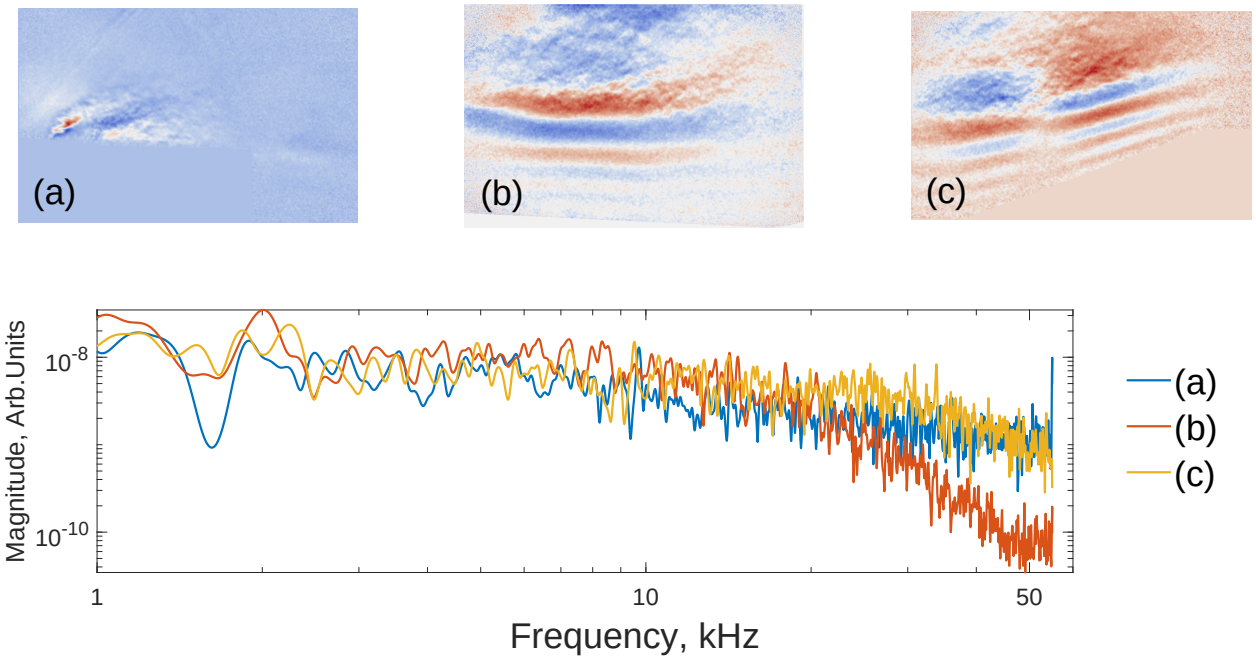


Fig. 12 Third-highest-energy mode in the POD of the (a) camera 1a position, (b) camera 2 position, and (c) camera 3 position with the spectra given for each.

3. DMD Analysis of SAFS Data

Eight notable DMD modes ordered by ascending frequency from camera position 1a for the fuel-on, flame-on run condition are shown in Fig. 13. Here, Fig. 13a shows a similar mode to the POD mode in Fig. 10a occurring at 1.0 kHz. From both the still image and when viewed as an image sequence, a 3-feature coupling can be deduced. An oscillation in

the shock, an oscillation in the injection plume, and an expansion wave type feature can all be observed. While causality is difficult to determine, it is likely that either the oscillating shock is causing varying post-shock flow parameters that cause the injection to oscillate, or an oscillation in the injection system supply is causing the shock to oscillate. One of these coupled motions then causes a different downstream Mach number which leads to changing intensity in the expansion wave around the corner. Figures 13b and c, show similar features to Fig. 13a, and could be either harmonics or a combination of modes, however the shock is less correlated in both of these modes. In Figs. 13d, e, f, g, and h, the injection site seems to contain difficult to interpret phase information. In Fig. 13d at 22.3 kHz there is phase information related to the expansion around the corner while in Fig. 13e at 22.17 kHz contains large waves that seem to propagate from the injection site downstream. Figs. 13f, g, and h at 40.6 kHz, 49.7 kHz, and 51.9 kHz, respectively, all contain a single set of out of phase waves underneath the injection plume that impinges on the surface before reaching the corner, but other motion is difficult to distinguish.

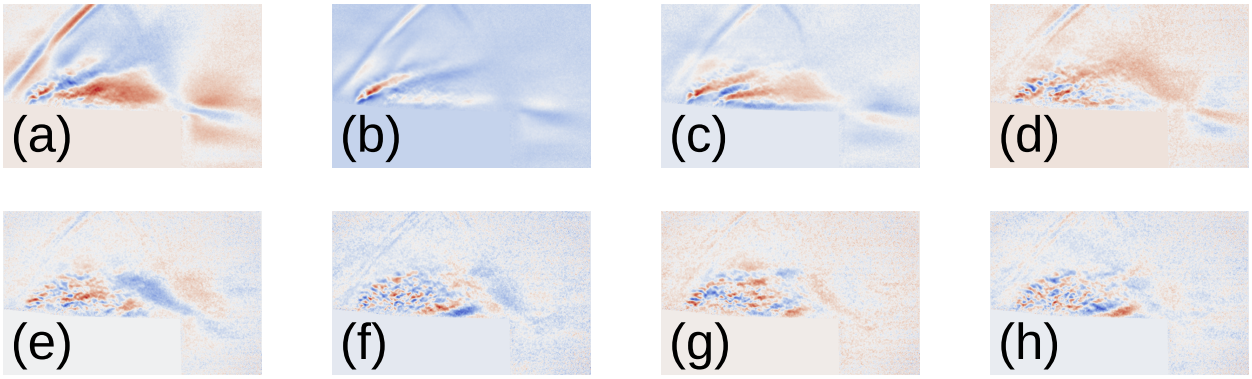


Fig. 13 Notable DMD modes at position 1a for the fuel-on, flame-on run condition at (a) 1.0 kHz, (b) 1.1 kHz, (c) 2.1 kHz, (d) 7.95 kHz, (e) 22.17 kHz, (f) 40.6 kHz, (g) 49.7 kHz, and (h) 51.9 kHz.

Eight notable DMD modes ordered by ascending frequency from camera position 2 for the fuel-on, flame-on run condition are shown in Fig. 14. In Figs. 14a and b both show downward propagating wave-like structures at 15.6 kHz and 20.6 kHz, respectively, similar to the waves seen in the POD for camera position 2. Fig. 14c shows wave-like motion in the injection plume that moves from left to right and is correlated with waves that propagate downward to the test section boundary at 20.6 kHz. Figures 14d, e, f, and g at 28 kHz, 31.3 kHz, 34.5 kHz, and 44.5 kHz respectively, show diagonal waves propagating from the top left of the field of view to the bottom right. These could be associated the turning of the flow around the corner or geometry change in the test section. Figure 14h is an example of high frequency chaotic noise at 51.9 kHz that is difficult to interpret.

Eight notable DMD modes ordered by ascending frequency from camera position 3 at the fuel-on, flame-on run condition are shown in Fig. 15. Figure 15a at 0.70 kHz shows a large oscillation in the injection plume but is not strongly

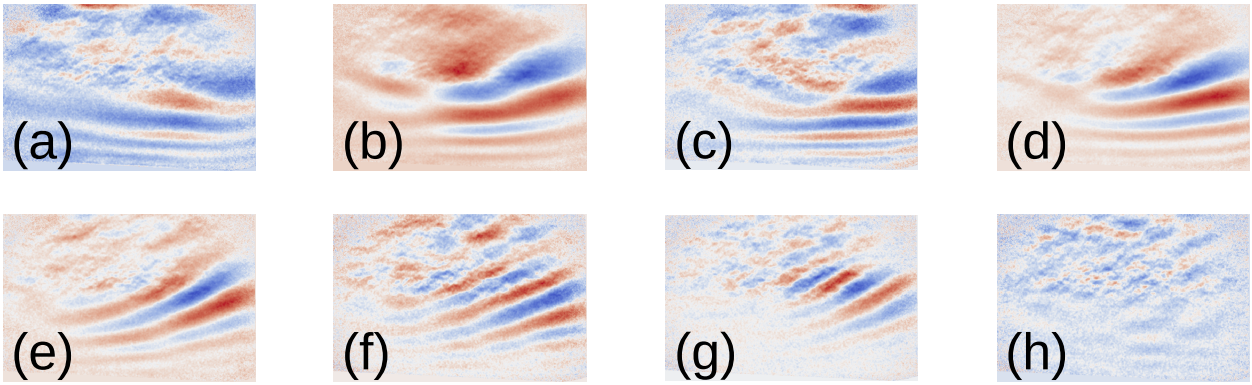


Fig. 14 Notable DMD modes at position 2 for the fuel-on, flame-on run condition at (a) 15.6 kHz, (b) 17.5 kHz, (c) 20.6 kHz, (d) 28 kHz, (e) 31.3 kHz, (f) 34.5 kHz, (g) 44.5 kHz, and (h) 51.9 kHz.

correlated to motion near the bottom of the cavity. While the frequencies don't quite match, it is close to the frequency seen in Fig. 13a and could be a downstream effect of the 3-feature coupling. Figure 15b shows a downward propagating wave that is correlated to disturbances in the injection plume at 12.3 kHz. Figures 15c, d, e, g, and h all show some wave-like structure that propagates at an angle to the test section boundary at 12.7 kHz, 19 kHz, 24.2 kHz, 51.9 kHz, and 52.3 kHz, respectively. Interestingly this feature is apparent across a wide range of frequencies with the only major change in shape being the thickness of the phase-correlated regions. As the frequency increases, the thickness tends to decrease. These modes could be harmonics of combinations of modes that share spatial coherence. Figre 15f at 38.1 kHz is an example of weakly correlated chaotic movement in the injection plume that also weakly correlates to an angled wave onto the bottom test section boundary. While difficult to interpret the injection plume motion, it seems that turbulent motion in the plume is somehow connected to the downward propagating waves.

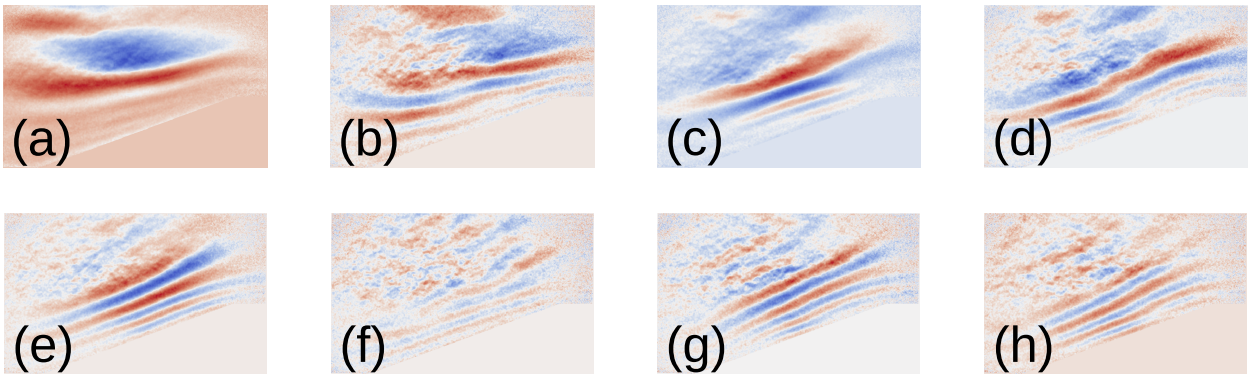


Fig. 15 Notable DMD modes at position 3 for the fuel-on, flame-on run condition at (a) 0.70 kHz, (b) 12.3 kHz, (c) 12.7 kHz, (d) 19 kHz, (e) 24.2 kHz, (f) 38.1 kHz, (g) 51.9 kHz, and (h) 52.3 kHz.

D. Air Throttle

1. Comparison of SAFS and OH PLIF Data

Figure 16 shows a stitched SAFS single-shot image from the positions 1a, 2, and 3 fields-of-view while maintaining a global equivalence ratio of $\phi = 0.18$ and with the air throttle used to shift the shock train into the isolator. In this image, the shocks that were observed in Fig. 7 without the air throttle are no longer observed. This is likely because the shock train was larger, slowing the flow to a subsonic condition ahead of the injectors. Additionally, the signature of the plume extending downstream over the cavity appears stronger. When viewing the entire image sequence, the wavelength of the wave-like structures appears to be larger than that observed for the fuel-on, flame-on condition with no air throttle. Also, nodal regions within the wave-like structures were observed intermittently.

Figure 17a shows a stitched single-shot image from the positions 1a and 2 fields-of-view acquired with the OH PLIF imaging system. Here, strong gradients in OH PLIF intensity indicate flame edges near the top of the cavity. When viewing a sequence of single-shot images of the PLIF data from this condition, OH is more uniform and persistent near the floor of the cavity, unlike the condition where the air throttle was off as in Fig. 8. Moreover, flame edges are confined to the shear layer region, rather than occurring in the cavity. Figure 17b shows a time-average OH PLIF image, again showing the OH confined to the cavity throughout the full image sequence. Intensity variations are once again due to the non-uniformity of the laser sheet. In the position 2 field-of-view, the average OH PLIF signal extends from the floor and is strong at the height of the cavity step, whereas the average is angled downward similar to the fuel-on, flame-on condition in Fig. 8b. Differences in flame angle between conditions are complemented by the SAFS images. The slightly higher penetration angle and penetration depth of the fuel jet seen in Fig. 7, as well the disappearance of the reflected shock impinging in the jets near the cavity step, likely produce different local fuel mixing conditions and thus flame stabilization locations.

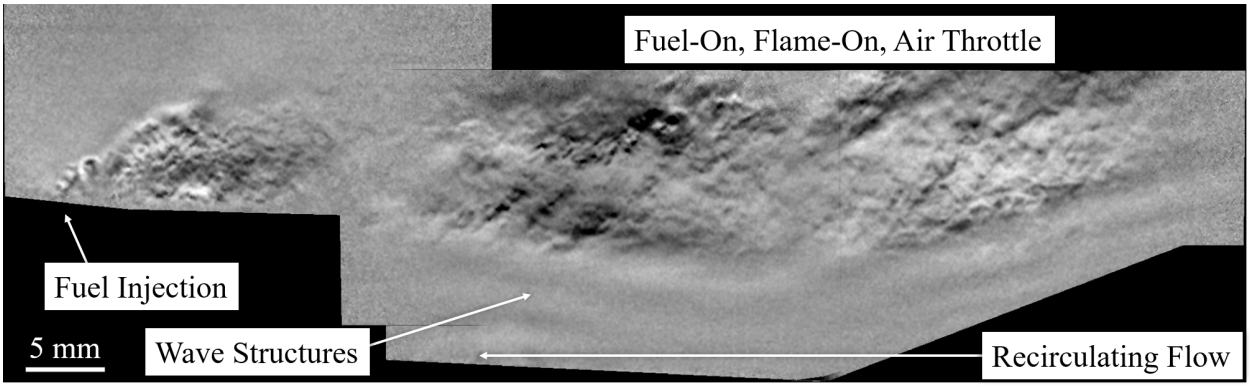
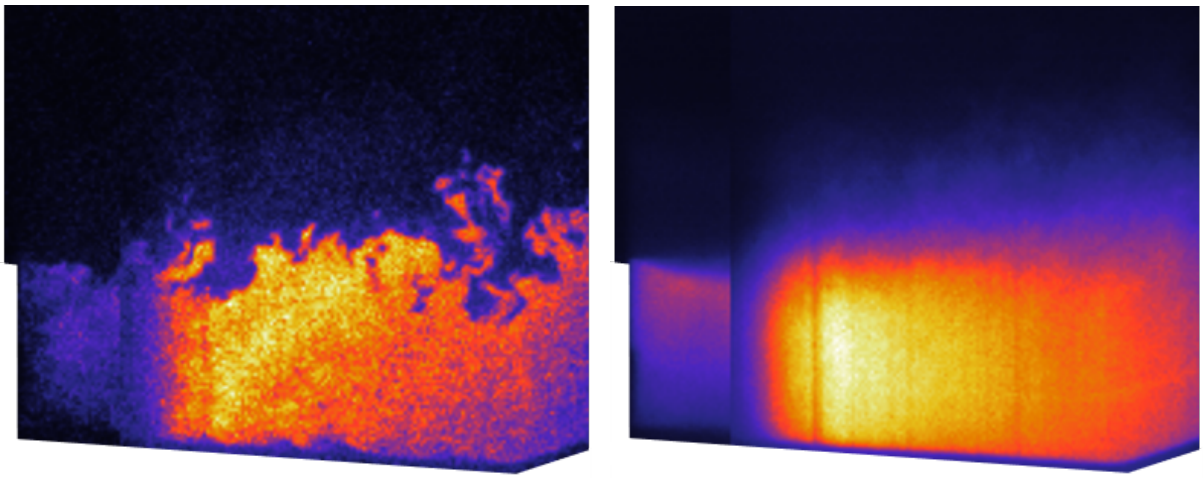


Fig. 16 Stitched single-shot image and from a sequence of 4096 single-shot images acquired with fuel injection on, flame on, and air throttle on.



(a) **(b)**

Fig. 17 Stitched (a) single-shot image and (b) time-average image from a sequence single-shot OH PLIF images acquired with fuel injection, flame, and air throttle.

2. POD Analysis of SAFS Data

The energy fractions of the top ten POD modes for each camera position at the air throttle run condition are shown in Fig. 18. Note that the energies contained in the first mode for each position vary significantly from one another, which is in stark contrast to the fuel-on, flame-on run condition where first mode energies were essentially the same. For this run condition, the flow captured by the cameras at positions 1a and 2 has a steeper drop in energy from the first to second mode than the camera at position 3. Further, the flow at position 2 has a steeper drop off from the first to third highest energy mode than the flow at position 1a. Additionally, the energy reduction from mode to mode becomes relatively flat for position 2 after the third mode and for position 1a after the fourth mode. This means that, likely, most of the important variance in the data for positions 2 and 1a is captured in the first three and four modes, respectively. For position 3, the modes exhibit a steady drop in energy. This could mean that there are multiple important modes or that the flow here is chaotic with no correlations. As will be shown later, there are dominant mode shapes and frequency peaks in both the POD and DMD for position 3 and so the following POD discussion for each camera position is limited to the top three modes for brevity.

The POD mode with the most energy at the air throttle run condition for camera positions 1a, 2, and 3 is shown in Figs. 19a, 19b, and 19c, respectively with the associated frequency spectra. In each of the POD images large out-of-phase structures are present. In Fig. 19a, an oscillation that seems to stem from fuel injection dominates the field of view. In

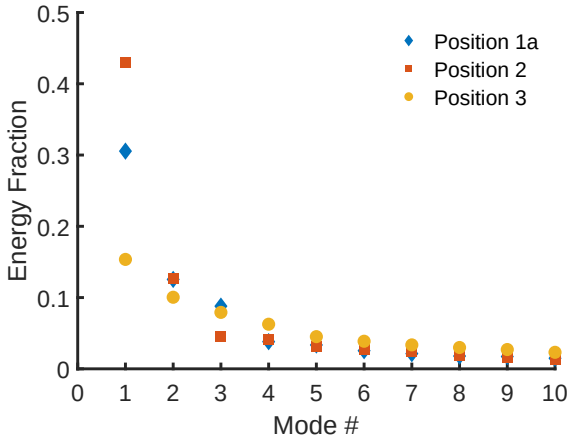


Fig. 18 Top ten POD mode energy fractions of each camera position at the air throttle run condition.

both Figs. 19b and 19c, the oscillation seems to have split into two packets and there seem to be weakly correlated disturbances propagating downward to the test section wall in the same fashion as Figs. 10b and c. The downward propagating waves seem to roughly be in phase with themselves for each of the position 2 and position 3 locations, as no anti-correlated sections are seen in the bottom half of the images. The spectra contain notable peaks at 44.6 kHz, 51.5 kHz, and 54 kHz for the camera 1a position (a), 28.2 kHz, 43.5 kHz, 48.9 kHz, and 55 kHz for the camera 2 position (b), and 21.8 kHz, 32 kHz, 48.9 kHz, and 55 kHz for the camera 3 position (c). Notably, the spectra includes large peaks at 55 kHz, the Nyquist cutoff frequency, and this peak will be seen again in the later sections.

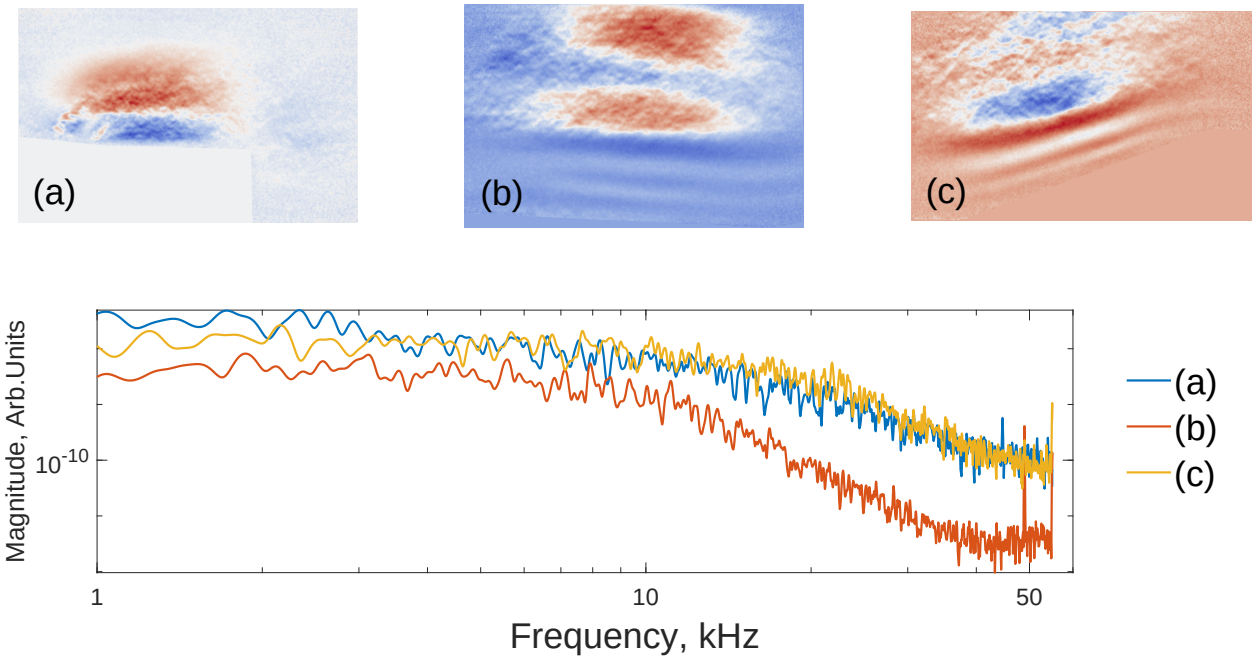


Fig. 19 Modes with the highest energy at the air throttle run condition POD of the (a) camera 1a position, (b) camera 2 position, and (c) camera 3 position with the spectra given for each.

The second-highest-energy POD mode at the air throttle run condition for camera positions 1a, 2, and 3 is shown in Figs. 20a, 20b, and 20c, respectively with the associated frequency spectra. In Fig. 20a, a single structure that oscillates with respect to the rest of the field of view is seen, which could indicate a puffing type of oscillation. The flow observed from the camera at position 2 20b and position 3 20c shows large scale oscillations similar to those seen in Fig. 20b and Fig. 20c, but the downward propagating waves are less defined. The spectra contain notable peaks at 25 kHz, 32 kHz,

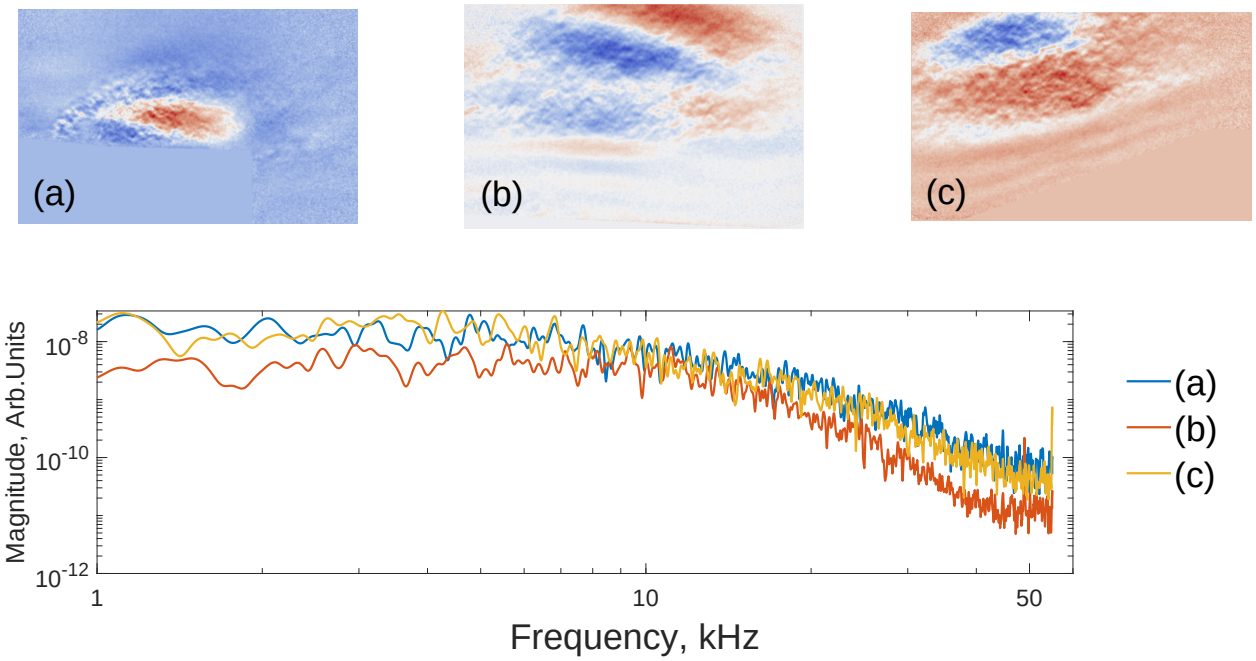


Fig. 20 Second-highest-energy mode in the POD of the (a) Camera 1a position, (b) Camera 2 position, and (c) Camera 3 position with the spectra given for each.

and 44.7 kHz for the camera 1a position (a), 28.7 kHz, 42.6 kHz, 44.6 kHz, and 48.9 kHz for the camera at position 2 (b), and 30.8 kHz and 55 kHz for the camera at position 3 (c).

The third-highest-energy POD mode at the air throttle run condition for camera positions 1a, 2, and 3 is shown in Figs. 21a, 21b, and 21c, respectively with the associated frequency spectra. In Fig. 21a the mode shows two correlated and two anti-correlated packets near the fuel injection site. In Fig. 21b and Fig. 21c the oscillations in the upper part of the flow are more strongly correlated with the downward propagating waves which themselves have correlated and anti-correlated regions. The spectra contain notable peaks at 44.6 kHz and 46.7 kHz for the camera at position 1a (a), 7.9 kHz and 35.4 kHz for the camera at position 2 (b), and 21.8 kHz and 32.1 kHz for the camera at position 3 (c).

3. DMD Analysis of SAFS Data

Eight notable DMD modes ordered by ascending frequency from camera position 1a for the air throttle run condition are shown in Fig. 22. Here, Fig. 22a shows a similar mode the the POD mode in Fig. 19a and occurs at a frequency of 0.685 kHz. Figure 22b shows what could be a harmonic of Fig. 22a at 1.337 kHz. Figures 22c, e, and f show what look like packets of correlated and anti-correlated information originating from the injection site at 12.6 kHz, 24.5 kHz, and 26.5 kHz. These could be a puffing or waving oscillatory motion and could be a harmonic of Fig. 22c. Figure 22d seems to show oscillations that are correlated with both the fuel injection and what looks like expansion waves around the corner at 22.3 kHz. Figure 22g shows angled waves that, when viewed as an image sequence, stay connected similar to Fig. 22d and unlike those in Figs. 22c,e, and f. Figure 22h is included as an example of a mode appearing at the Nyquist cutoff, which could be related to the peaks in the POD at 55 kHz. Inspection of the mode seems to show chaotic phase information and is difficult to ascertain meaning from. This could mean the peaks in the POD at 55 kHz are noise or extremely random turbulent action in the flow.

Figure 23 shows eight notable DMD modes ordered by ascending frequency from the flow at camera position 2 for the air throttle run condition. In Figs. 23a and b, the flow exhibits low frequency motion that moves from left to right in the top of the image that is correlated to waves that propagate downward in the bottom half of the image at 2.1 kHz and 3.3 kHz, respectively. Figure 23c shows a similar pattern to the bottom half of Fig. 23a and Fig. 23b, but it exists in the full flow field at 13.2 kHz. Figs. 23d, e, and f all show a diagonal wave-like pattern that exists in the upper part of the field of view, in the injection plume at frequencies 21 kHz, 28 kHz, and 42.9 kHz. Figures 23d and f could be harmonics of each other and have more strongly delineated phase transitions than Fig. 23e, where the phase information is chopped

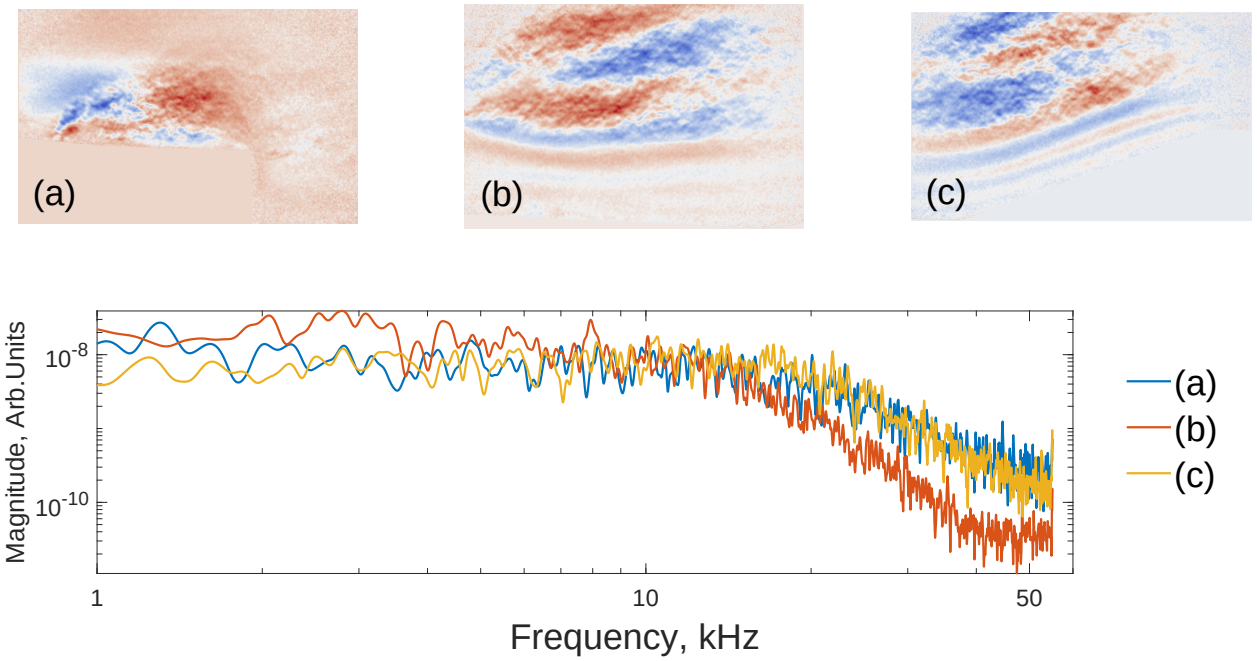


Fig. 21 Third-highest-energy mode in the POD of the (a) Camera 1a position, (b) Camera 2 position, and (c) Camera 3 position with the spectra given for each.

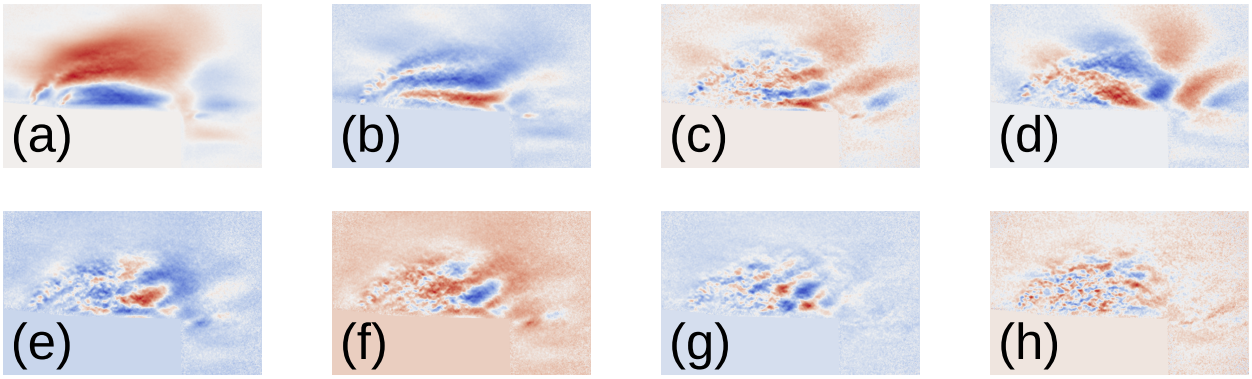


Fig. 22 Eight notable DMD modes from camera position 1a at (a) 0.685 kHz, (b) 1.337 kHz, (c) 12.6 kHz, (d) 22.3 kHz, (e) 24.5 kHz, (f) 26.5 kHz, (g) 51.8 kHz, and (h) 54.99 kHz.

into pieces. Figures 23g and h are examples of high frequency content at 51.2 kHz and 51.9 kHz that when viewed as an image sequence is difficult to identify motion, but rather looks like the correlated and anti-correlated regions simply flash in and out of phase with each other.

Figure 24 shows eight notable DMD modes from the flow at camera position 3 for the air throttle run condition. In Figs. 24a and b, the flow there is relatively low frequency oscillation in the injection plume at 1.2 kHz and 8.2 kHz, respectively. In Figs. 24c and e, there are regions in the injection plume that are correlated with waves that impinge on the bottom of the test section, at 14.7 kHz and 24.8 kHz, respectively. This motion is slightly different than that of Figs. 24d and f, there there are long boomerang shaped waves that traverse the injection plume from left to right and ultimately impinge downward onto the bottom of the test section at 20 kHz and 26.5 kHz, respectively. In Figs. 24g and h, there are thin, diagonal wave-like patterns at 37.1 kHz and 52.6 kHz, however the high frequency mode in Fig. 24h when viewed as an image sequence, does not exhibit easily interpretable motion while Fig. 24g does. Figure 24h differs slightly than previous high frequency chaotic motion in that it has clearly delineated regions of phase and so might be an actual oscillatory mode that describes some turbulent function in the flow.

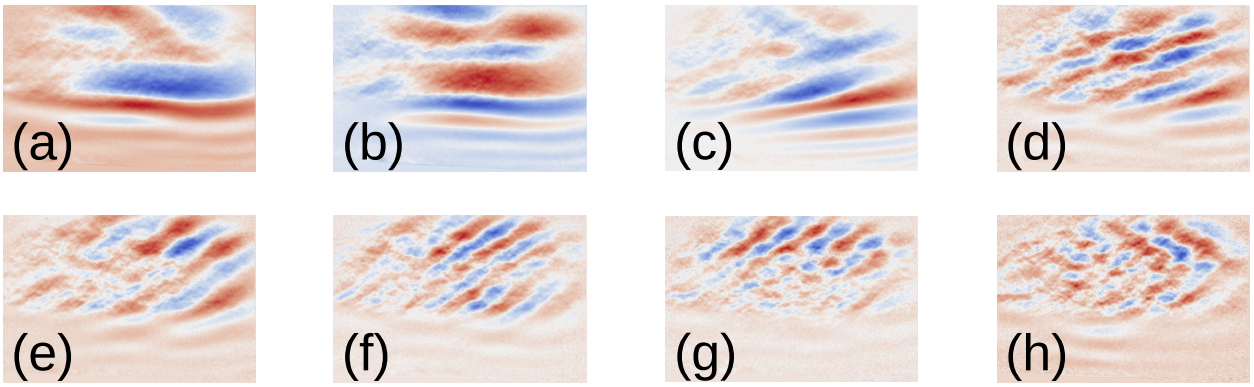


Fig. 23 Eight notable DMD modes from camera position 2 at (a) 2.1 kHz, (b) 3.3 kHz, (c) 13.2 kHz, (d) 21 kHz, (e) 28 kHz, (f) 42.9 kHz, (g) 51.2 kHz, and (h) 51.9 kHz.

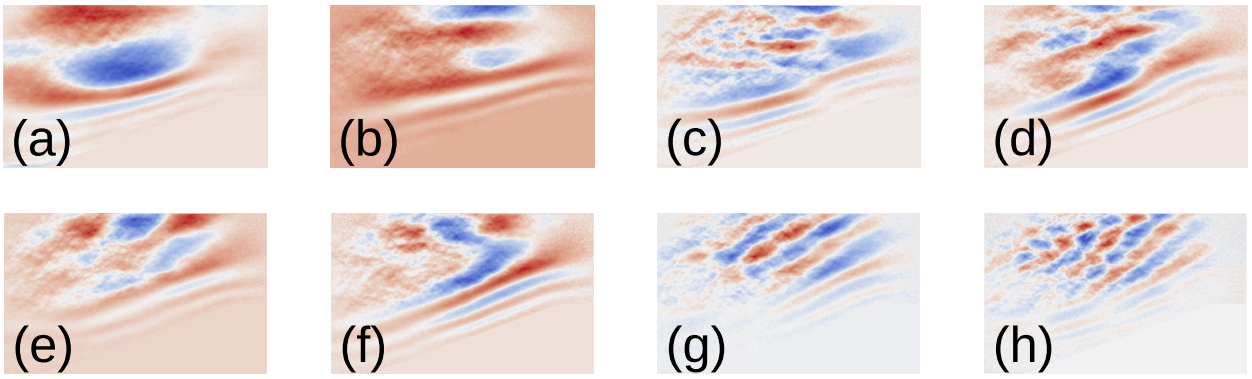


Fig. 24 Eight notable DMD modes from camera position 3 at (a) 1.2 kHz, (b) 8.2 kHz, (c) 14.7 kHz, (d) 20 kHz, (e) 24.8 kHz, (f) 26.5 kHz, (g) 37.1 kHz, and (h) 52.6 kHz.

V. Conclusion

In this work, a high-speed self-aligned focusing schlieren system was used to visualize flow in the University of Virginia Supersonic Combustion Facility. This was the first application of this method in the facility. Image sequences for four different run conditions were obtained: 1) fuel-off, flame-off, 2) fuel-on, flame-off, 3) fuel-on, flame-on, and 4) fuel-on, flame-on with air throttle. Significant differences were observed in the schlieren image sequences for each of these run conditions. Planar laser-induced fluorescence images of OH acquired at 20 Hz were also captured for the conditions with fuel injection and flame, both with and without the use of an air throttle to control shock train position. The images obtained using the self-aligned focusing schlieren method indicated the presence of wave-like structures within the combustor cavity that corresponded to the location of OH. When the air throttle was engaged, the wavelength of these structures were observed to increase.

The time-resolved SAFS visualizations allowed for both proper orthogonal decomposition and dynamic mode decomposition analyses to be performed. These methods enable dominant coherent structures and their corresponding frequencies to be identified that might otherwise not be apparent when viewing a single-shot image or even an entire sequence of images. In this work, the modal analysis methods were used to describe the periodic motion of flow structures observed in both the fuel-on, flame-on and fuel-on, flame-on with air throttle run conditions. This included oscillations in the fuel plume near the point of injection, oscillations in the downstream plume within the primary flow path, and wave-like structures in the combustor cavity.

Acknowledgments

The authors would like to acknowledge NASA's Transformational Tools & Technologies (TTT) project for their support and NASA's Hypersonics Technology Project (HTP) for their support of Nicholas Mejia. Support for the work at UVA was provided by the Defense Advanced Research Projects Agency Grant #HR00112010014.

Disclosures

In this work, specific vendor and manufacturer names are explicitly mentioned only to accurately describe the test hardware. The use of vendor and manufacturer names does not imply endorsement by the U.S. Government. U.S. Patent #11,650,151 applies to the self-aligned schlieren system presented in this work.

References

[1] Gauba, G., Klavuhn, K. G., McDaniel, J. C., Victor, K. G., Krauss, R. H., and Whitehurst, R. B., "OH Planar Laser-Induced Fluorescence Velocity Measurements in a Supersonic Combustor," *AIAA Journal*, Vol. 35, No. 4, 1997, pp. 678–686. https://doi.org/10.2514/2.157.

[2] McRae, C., Johansen, C., Danehy, P., Gallo, E., Cantu, L., Magnotti, G., Cutler, A., Rockwell, R., Goyne, C., and McDaniel, J., "OH PLIF Visualization of the UVa Supersonic Combustion Experiment: Configuration C," *51st AIAA Aerospace Sciences Meeting including the New Horizons Forum and Aerospace Exposition*, American Institute of Aeronautics and Astronautics, 2013. https://doi.org/10.2514/6.2013-34.

[3] Johansen, C. T., McRae, C. D., Danehy, P. M., Gallo, E. C. A., Cantu, L. M. L., Magnotti, G., Cutler, A. D., Rockwell, R. D., Goyne, C. P., and McDaniel, J. C., "OH PLIF visualization of the UVa supersonic combustion experiment: configuration A," *Journal of Visualization*, Vol. 17, No. 2, 2014, pp. 131–141. https://doi.org/10.1007/s12650-014-0197-2.

[4] Cantu, L. M. L., Gallo, E. C. A., Cutler, A. D., Danehy, P. M., Rockwell, R. D., Johansen, C. T., Goyne, C. P., and McDaniel, J. C., "OH PLIF Visualization of a Premixed Ethylene-fueled Dual-Mode Scramjet Combustor," *54th AIAA Aerospace Sciences Meeting*, American Institute of Aeronautics and Astronautics, 2016. https://doi.org/10.2514/6.2016-1763.

[5] Geipel, C. M., Rockwell, R. D., Chelliah, H. K., Cutler, A. D., Spelker, C. A., Hashem, Z., and Danehy, P. M., "High-Resolution OH and CH2O Visualization in a Premixed Cavity-Anchored Ethylene-Air Flame in a M = 0.6 Flowfield," *10th U.S. National Combustion Meeting Organized by the Eastern States Section of the Combustion Institute*, 2017.

[6] Geipel, C. M., Rockwell, R., Chelliah, H., Cutler, A. D., Spelker, C., Hashem, Z., and Danehy, P. M., "High-Spatial-Resolution OH PLIF Visualization in a Cavity-Stabilized Ethylene-Air Turbulent Flame," *33rd AIAA Aerodynamic Measurement Technology and Ground Testing Conference*, American Institute of Aeronautics and Astronautics, 2017. https://doi.org/10.2514/6.2017-3901.

[7] Geipel, C. M., Cutler, A. D., Rockwell, R. D., and Chelliah, H. K., "Characterization of Flame Front Structure in a Dual-Mode Scramjet Combustor with OH-PLIF," *AIAA Scitech 2019 Forum*, American Institute of Aeronautics and Astronautics, 2019. https://doi.org/10.2514/6.2019-0831.

[8] Metro, A. J., Kim, A., Rockwell, R. D., Elkowitz, L. A., Dedic, C. E., and Cutler, A. D., "OH imaging of partially-premixed ethylene-air flames in a dual-mode scramjet," *AIAA SCITECH 2023 Forum*, American Institute of Aeronautics and Astronautics, 2023. https://doi.org/10.2514/6.2023-2434.

[9] Allison, P., Frederickson, K., Kirik, J. W., Rockwell, R. D., Lempert, W. R., and Sutton, J. A., "Investigation of Flame Structure and Combustion Dynamics using CH2O PLIF and High-Speed CH* Chemiluminescence in a Premixed Dual-Mode Scramjet Combustor," *54th AIAA Aerospace Sciences Meeting*, American Institute of Aeronautics and Astronautics, 2016. https://doi.org/10.2514/6.2016-0441.

[10] Allison, P. M., Frederickson, K., Kirik, J. W., Rockwell, R. D., Goyne, C. P., Lempert, W. R., and Sutton, J. A., "Flame Structure and Dynamics in a Premixed Dual-Mode Scramjet Combustor from Fluorescence Imaging," *Journal of Propulsion and Power*, Vol. 35, No. 3, 2019, pp. 552–564. https://doi.org/10.2514/1.b37057.

[11] Kirik, J. W., Goyne, C. P., McDaniel, J. C., and Rockwell, R. D., "Aerodynamics of Lean Blowout in a Premixed Dual-Mode Scramjet," *Journal of Propulsion and Power*, Vol. 34, No. 3, 2018, pp. 819–822. https://doi.org/10.2514/1.b36814.

[12] Kouchi, T., Goyne, C., Rockwell, R., Reynolds, R., Krauss, R., and McDaniel, J., "Focusing-schlieren Visualization in Direct-connect Dual-mode Scramjet," *18th AIAA/3AF International Space Planes and Hypersonic Systems and Technologies Conference*, American Institute of Aeronautics and Astronautics, 2012. https://doi.org/10.2514/6.2012-5834.

[13] Kouchi, T., Goyne, C. P., Rockwell, R. D., and McDaniel, J. C., "Focusing-schlieren visualization in a dual-mode scramjet," *Experiments in Fluids*, Vol. 56, No. 12, 2015. https://doi.org/10.1007/s00348-015-2081-9.

[14] Hartmann, J., "The Acoustic Air-Jet Generator," Technical Translation (2021) NASA-TT-20210016495, Nov. 1940.

[15] Schardin, H., "Schlieren methods and their applications," NASA-TT-F12731 (1970), 1942.

[16] Burton, R. A., "A Modified Schlieren Apparatus for Large Areas of Field," *Journal of the Optical Society of America*, Vol. 39, No. 11, 1949, p. 907. https://doi.org/10.1364/josa.39.000907.

[17] Weinstein, L. M., "Large-field high-brightness focusing schlieren system," *AIAA Journal*, Vol. 31, No. 7, 1993, pp. 1250–1255. https://doi.org/10.2514/3.11760.

[18] Settles, G. S., *Schlieren and Shadowgraph Techniques: Visualizing Phenomena in Transparent Media*, Springer Berlin Heidelberg, 2001. https://doi.org/10.1007/978-3-642-56640-0.

[19] Bathel, B. F., and Weisberger, J. M., "Compact, self-aligned focusing schlieren system," *Optics Letters*, Vol. 46, No. 14, 2021, pp. 3328–3331. https://doi.org/10.1364/ol.428011.

[20] Weisberger, J. M., and Bathel, B. F., "Single source/cutoff grid, self-aligned focusing schlieren system," *Experiments in Fluids*, Vol. 63, No. 1, 2022. https://doi.org/10.1007/s00348-022-03389-7.

[21] Rockwell, R. D., Goyne, C. P., Chelliah, H., McDaniel, J. C., Rice, B. E., Edwards, J. R., Cantu, L. M. L., Gallo, E. C. A., Cutler, A. D., and Danehy, P. M., "Development of a Premixed Combustion Capability for Dual-Mode Scramjet Experiments," *Journal of Propulsion and Power*, Vol. 34, No. 2, 2018, pp. 438–448. https://doi.org/10.2514/1.b36550.

[22] Taira, K., Brunton, S. L., Dawson, S. T. M., Rowley, C. W., Colonius, T., McKeon, B. J., Schmidt, O. T., Gordeyev, S., Theofilis, V., and Ukeiley, L. S., "Modal Analysis of Fluid Flows: An Overview," *AIAA Journal*, Vol. 55, No. 12, 2017, pp. 4013–4041. https://doi.org/10.2514/1.j056060.

[23] Bakewell, H. P., and Lumley, J. L., "Viscous Sublayer and Adjacent Wall Region in Turbulent Pipe Flow," *The Physics of Fluids*, Vol. 10, No. 9, 1967, pp. 1880–1889. https://doi.org/10.1063/1.1762382.

[24] Berkooz, G., Holmes, P., and Lumley, J. L., "The proper orthogonal decomposition in the analysis of turbulent flows," *Annual review of fluid mechanics*, Vol. 1, No. 25, 1993, pp. 539–575. https://doi.org/10.1146/annurev.fl.25.010193.002543.

[25] Bathel, B. F., Litzner, C. R., Jones, S. B., Berry, S. A., Smith, N. T., and Garbeff, T. J., "High-Speed Schlieren Analysis of Retropropulsion Jet in Mach 10 Flow," *Journal of Spacecraft and Rockets*, Vol. 57, No. 1, 2020, pp. 33–48. https://doi.org/10.2514/1.a34522.

[26] Marwege, A., and Gülhan, A., "Unsteady Aerodynamics of the Retropropulsion Reentry Burn of Vertically Landing Launchers," *Journal of Spacecraft and Rockets*, 2023, pp. 1–15. https://doi.org/10.2514/1.a35647.

[27] Mejia, N. A., and Schmidt, B. E., "Experimental Investigation of Flow Interaction Dynamics in Supersonic Retropropulsion," *Journal of Spacecraft and Rockets*, Vol. 59, No. 5, 2022, pp. 1753–1762. https://doi.org/10.2514/1.a35228.

[28] Chen, L.-W., Wang, G.-L., and Lu, X.-Y., "Numerical investigation of a jet from a blunt body opposing a supersonic flow," *Journal of Fluid Mechanics*, Vol. 684, 2011, pp. 85–110.

[29] Schmid, P. J., "Dynamic mode decomposition of numerical and experimental data," *Journal of Fluid Mechanics*, Vol. 656, No. 1, 2010, pp. 5–28.

[30] Chen, K. K., Tu, J. H., and Rowley, C. W., "Variants of Dynamic Mode Decomposition: Boundary Condition, Koopman, and Fourier Analyses," *Journal of Nonlinear Science*, Vol. 22, No. 6, 2012, pp. 887–915. https://doi.org/10.1007/s00332-012-9130-9.

[31] Kou, J., and Zhang, W., "An improved criterion to select dominant modes from dynamic mode decomposition," Vol. 62, 2017, pp. 109–129. https://doi.org/10.1016/j.euromechflu.2016.11.015.

[32] Jovanović, M. R., Schmid, P. J., and Nichols, J. W., "Sparsity-promoting dynamic mode decomposition," Vol. 26, 2014. https://doi.org/10.1063/1.4863670.

[33] Dawson, S. T. M., Hemati, M. S., Williams, M. O., and Rowley, C. W., "Characterizing and correcting for the effect of sensor noise in the dynamic mode decomposition," *Experiments in Fluids*, Vol. 57, No. 3, 2016. https://doi.org/10.1007/s00348-016-2127-7.

[34] Hemati, M. S., Rowley, C. W., Deem, E. A., and Cattafesta, L. N., "De-biasing the dynamic mode decomposition for applied Koopman spectral analysis of noisy datasets," *Theoretical and Computational Fluid Dynamics*, Vol. 31, No. 4, 2017, pp. 349–368. https://doi.org/10.1007/s00162-017-0432-2.

[35] Proctor, J. L., Brunton, S. L., and Kutz, J. N., "Dynamic Mode Decomposition with Control," *SIAM Journal on Applied Dynamical Systems*, Vol. 15, No. 1, 2016, pp. 142–161. https://doi.org/10.1137/15m1013857.

[36] Sashidhar, D., and Kutz, J. N., "Bagging, optimized dynamic mode decomposition for robust, stable forecasting with spatial and temporal uncertainty quantification," Vol. 380, 2022. https://doi.org/10.1098/rsta.2021.0199.

[37] Askham, T., and Kutz, J. N., "Variable Projection Methods for an Optimized Dynamic Mode Decomposition," Vol. 17, 2018, pp. 380–416. https://doi.org/10.1137/m1124176.

[38] Zhang, H., Rowley, C. W., Deem, E. A., and Cattafesta, L. N., "Online Dynamic Mode Decomposition for Time-Varying Systems," *SIAM Journal on Applied Dynamical Systems*, Vol. 18, No. 3, 2019, pp. 1586–1609. https://doi.org/10.1137/18m1192329.

[39] Schmid, P. J., "Dynamic Mode Decomposition and Its Variants," *Annual Review of Fluid Mechanics*, Vol. 54, No. 1, 2022, pp. 225–254. https://doi.org/10.1146/annurev-fluid-030121-015835.

[40] Erichson, N. B., Mathelin, L., Kutz, J. N., and Brunton, S. L., "Randomized Dynamic Mode Decomposition," *SIAM Journal on Applied Dynamical Systems*, Vol. 18, No. 4, 2019, pp. 1867–1891. https://doi.org/10.1137/18m1215013.